

1. Geological backgrounds of the CLP source regions

Two different geological units have been proposed as the ultimate source of the aeolian dust: the south-central segments of the CAOB to the northwest and the NTP to the west. The south-central segments of the CAOB contain several microcontinental blocks with Archean to Neoproterozoic crystalline basement that were welded through a long accretionary history mainly in the Paleozoic. Orogenic convergence resulted in episodic magmatism through the period from 550 to 200 Ma (Sun et al., 2008, 2009; Li et al., 2013; Cai et al., 2015; He et al., 2018), granulite-amphibolite facies metamorphism at 390–360 Ma (Kozakov et al., 2007), and eclogite to granulite-amphibolite facies metamorphism from 310 to 265 Ma (Zhao et al., 2018).

In contrast to the CAOB, the NTP consists of several continental blocks and intervening orogenic belts that record the subduction and closure of the Proto-Tethys and Neo-Tethys Oceans. Basement rocks of these continental blocks are mainly Neoproterozoic granitoids and metamorphic complexes with minor Neoproterozoic to Mesoproterozoic rocks. The NTP is geographically divided into two mountain ranges by the Qaidam Basin. In the northern portion, Early Paleozoic magmatism (550–420 Ma) and eclogite-blueschist facies metamorphism with metamorphic ages of ca. 490–420 Ma are documented in the North Qilian Orogen and North Qaidam metamorphic belt (Zuza et al., 2018). In the southern NTP, the emplacement of extensive igneous rock suites occurred in two stages, from 530 to 350 Ma and 270 to 200 Ma (Jiao et al., 2013; Zhai et al., 2013; Chen et al., 2014; Ding et al., 2014, 2015; Zhang et al., 2014; Peng et al., 2015; Xia et al., 2015; Xiong et al., 2015; Yu et al., 2015; Zhou et al., 2016; Cheng et al., 2017; Dong et al., 2018; Wang et al., 2018; Yang et al., 2015). Eclogite facies metamorphism at ca. 430–410 Ma was reported in the Kunlun Orogen, while Early Mesozoic eclogite-blueschist metamorphism and thick turbiditic strata were documented in the Qiangtang and Hoh Xil-Songpan-Ganzi terranes (Kapp et al., 2003; Song et al., 2018). The collision between India and Asia led to the extensive crustal shortening and topographical uplift of the NTP throughout the Cenozoic, resulting in pervasive volcanism and metamorphism to the south of the Qaidam Basin over the last 50 Ma (Kapp and DeCelles, 2019).

2. Samples and Analytical methods

The two samples from the western CLP were collected from the Wuchuancun (L1) and Qianjiatai (S1) sections (Fig. S1). Central CLP samples were taken from the well-studied Xifeng

section (Guo et al., 2001). They represent typical loess (glacial) and paleosol (interglacial) samples of the last glacial-interglacial cycle, with approximate deposition ages of 40–20 ka and 100–80 ka (Table S1). Approximately, 5 kg of sediment was collected from each locality. Mineral separation was carried out using standard heavy liquid and magnetic separation techniques before final hand picking under a binocular. To avoid sample bias, no attempt was made to exclude anhedral or inclusion-bearing grains; the mineral grains were selected from all recognizable populations. They were mounted in epoxy, and polished to approximately 2/3 to 1/2 thicknesses. Cathodoluminescence (CL) imaging and back-scattered electron (BSE) imaging for these grains were performed using a CAMECA SX-50 Electron Microprobe (Fig. S2). The working conditions during the CL imaging was 10 kV accelerating potential and during the BSE imaging was 15 kV accelerating potential.

Table S1. Location of the studied samples

Sample ID	Latitude	Longitude	Height	Region
W-L1	36.72508°N	104.08582°E	1819m	Wuchuancun, Baiyin
W-S1	35.11579°N	104.27341°E	2079m	Qianjiatai, Dingxi
C-L1	35.92347°N	107.62375°E	1512m	Xifeng, Qingyang
C-L1	35.92387°N	107.65248°E	1496m	Xifeng, Qingyang

2.1. Zircon U-Pb and Lu-Hf Isotope Analyses

Simultaneous U-Pb age and Lu-Hf isotope and measurements for W-L1 and -S1 were made in the Arctic Resources Laboratory (ARL) at the University of Alberta. The zircon samples were ablated using the laser ablation split stream (LASS) technique described by Yuan et al. (2008) and Xie et al. (2008) and refined by Fisher et al. (2011). RESOLUTION ArF 193 nm excimer laser ablation system was coupled with an Element XR sector field inductively coupled plasma-mass spectrometer (ICP-MS) and a Neptune Plus multi collector (MC)-ICP-MS. The zircons were ablated using a spot size of 50 μm , at a repetition rate of 6 Hz with the fluence regulated at $\sim 6.5\text{--}7\text{ J/cm}^2$. Zircon 91500 was employed as the primary standard for U-Pb mass bias fractionation and instrument drift correction, while the Plešovice, GJ-1 and LH94-15 zircons reference materials were employed as secondary standards. For Lu-Hf isotope analysis, two synthetic zircons with wide ranges of Yb/Hf ratios (MUN-1 and MUN-3) were analyzed for the correction of isobaric

interference of ^{176}Lu and ^{176}Yb on ^{176}Hf . Data reduction of LASS Lu-Hf + U-Pb in zircon analyses is conducted by newly developed features within *Iolite* software (Fisher et al., 2017).

Zircon dating and trace element analysis for LR was simultaneously analyzed by laser ablation (LA)-ICP-MS at the Key Laboratory of Crust-Mantle Materials and Environments, University of Science and Technology of China, Hefei, China. A pulsed 193 nm ArF excimer laser at a repetition ratio of 6 Hz, a beam diameter of 32 μm and laser fluence of 5.3 J/cm², coupled with an Agilent 7900 ICP-MS, was used for ablation. Helium was used as a carrier gas to transport the ablated material from the laser ablation cell to the ICP-MS. The signal was enhanced in the ICP-MS by addition of nitrogen in the central channel gas (Hu et al., 2008). Zircon 91500 was used as a reference standard to normalize isotopic fractionation; the reference material zircon GJ-1 was used for data quality monitoring.

Common Pb correction was applied using the method of Andersen (2002) and the data were treated with the ISOPLOT program of Ludwig (2012). Measurements of the Plešovice, GJ-1 and LH94-15 zircons yielded weighted mean U-Pb ages of 340.0 ± 0.9 Ma (MSWD [Mean Square Weighted Deviation] = 0.23; n=24), 601.8 ± 2.0 Ma (MSWD = 5.2; n=55) and 1819 ± 2.6 Ma (MSWD = 1.4; n=22). We have calculated the concordance as: (Concordance) = $(^{207}\text{Pb}/^{206}\text{Pb} \text{ age}) / (^{206}\text{Pb}/^{238}\text{U} \text{ age}) \times 100\%$ when $^{206}\text{Pb}/^{238}\text{U} \text{ age} > 1000$ Ma and (Concordance) = $(^{207}\text{Pb}/^{235}\text{U} \text{ age}) / (^{206}\text{Pb}/^{238}\text{U} \text{ age}) \times 100\%$ when $^{206}\text{Pb}/^{238}\text{U} \text{ age} < 1000$ Ma. The data were filtered by concordance within 85%~115%. $^{206}\text{Pb}/^{238}\text{U}$ ages are used for zircons younger than 1000 Ma, while $^{207}\text{Pb}/^{206}\text{Pb}$ ages were used for older grains. During the Hf isotopic analysis, the 91500, Plešovice, GJ-1 and LH94-15 zircons that used as the control standards yielded averaged $^{176}\text{Hf}/^{177}\text{Hf}$ ratios of 0.282300 ± 0.000029 (2SD [Standard Deviations]; n = 46), 0.282482 ± 0.000022 (2SD; n = 26), 0.282012 ± 0.000029 (2SD; n=22) and 0.281710 ± 0.000021 (SD; n=22), respectively. These results agree well with the recommended values within analytical uncertainties (Wiedenbeck et al., 1995; Fisher et al., 2017). Initial $^{176}\text{Hf}/^{177}\text{Hf}$ ratios for the zircon samples, denoted as $\epsilon_{\text{Hf}}(t)$, were calculated using a decay constant of $1.867 \times 10^{-11} \text{ yr}^{-1}$, a $^{176}\text{Hf}/^{177}\text{Hf}$ ratio of 0.282793 and a $^{176}\text{Lu}/^{177}\text{Hf}$ ratio of 0.0338 for the chondritic reservoir (Söderlund et al., 2004; Iizuka et al., 2015).

2.2. Monazite U-Th-Pb Isotope Analyses

The U-Th-Pb dating of monazite was performed by the LA-ICPMS at both the ARL at

University of Alberta and the State Key Laboratory of Geological Processes and Mineral Resources (GPMR), China University of Geosciences (CUG), Wuhan. We analyzed the monazite grains using a spot size of 16-24 μm , at a repetition rate of 4-5 Hz and a laser fluence of $\sim 3.5 \text{ J/cm}^2$ was employed. The Namaqualand or 44069 monazite was used as the primary standard while 117531 (Trebilcock) and KMD monazites were used as control standards. Data reduction was performed using the “Geochron_4” scheme of *Iolite* (Petrus and Kamber, 2012). We adopted $^{208}\text{Pb}/^{232}\text{Th}$ ages for further discussion as they ages are less likely to be affected by the presence of common Pb. In addition, we have calculated ^{207}Pb corrected $^{206}\text{Pb}/^{238}\text{U}$ ages for the unknown samples using a common Pb $^{207}\text{Pb}/^{206}\text{Pb}$ composition of 0.836, which is in excellent concordance with their $^{208}\text{Pb}/^{232}\text{Th}$ ages. The 117531 and KMD monazites yield weighted averaged $^{208}\text{Pb}/^{232}\text{Th}$ ages of $267.8 \pm 1.1 \text{ Ma}$ ($n = 32$; $\text{MSWD} = 0.49$) and $1802 \pm 6 \text{ Ma}$ ($n = 19$; $\text{MSWD} = 1.0$) during the analysis, which are in good agreement with the reported values in previous studies (Fisher et al., 2020). Concordance was calculated by $(^{207}\text{Pb} \text{ corrected } ^{206}\text{Pb}/^{238}\text{U} \text{ age}) / (^{208}\text{Pb}/^{232}\text{Th} \text{ age}) * 100\%$ and the data were filtered by concordance within 90%~110%. As radiogenic Pb content increases with age, young grains typically have proportionately greater age uncertainties. Hence, discordance up to 25% were permitted for monazite grains yielding ages younger than 100 Ma.

2.3. Rutile Trace element and U-Pb Isotope Analyses

Compositional analysis of detrital rutile of samples W-L1 and -S1 was acquired on an electron microprobe (Cameca SX100 [TCP/IP Socket]) equipped with 5 tunable wavelength dispersive spectrometers, at the University of Alberta. Analysis was operated under 40 degrees takeoff angle with a beam energy of 20 keV and beam current of 20 nA. Beam size was 5 microns for all elements. Elements were acquired using analyzing crystals LLIF for Ta la, Fe ka, W la, V ka, PET for Cr ka, Nb la, Zr la, Sn la, Ti ka, and LTAP for Al ka, Si ka. Critical discrimination between rutile, anatase, brookite and other minerals have been applied. Rutile are constrained by $\text{Si} < 300 \text{ ppm}$, $\text{V} > 10^{2.5} \text{ ppm}$, and $\text{Cr} > 100 \text{ ppm}$ (Triebold et al., 2011). For the discrimination of metapelitic and metamafic rutile, criteria proposed by Triebold et al. (2012) were applied (Fig. S4). The Zr-in-rutile thermometry is calculated by: $T(\text{K}) = (4470 \pm 120) / ([7.36 \pm 0.10] - \log[\text{Zr}(\text{ppm})])$ (Watson et al., 2006).

Rutile U-Pb dating of samples W-L1 and -S1 was performed by the LA-ICPMS at ARL, with a laser spot diameter of 50 μm , 5 Hz repetition and a laser fluence of $\sim 2 \text{ J/cm}^2$ on the same spots

used for trace element analysis. Rutile crystals R10 and R13 were employed as the primary and control standards, respectively (Luvizotto et al., 2009). Rutile U-Pb dating and trace element analysis for sample C-L1 and -S1 was simultaneously analyzed by LA-ICPMS at the GPMR. Rutile crystals R632 and DX01 were employed as the primary and control standards, respectively (Zhou et al., 2015; Axelsson et al., 2018). The reference material NIST SRM 610 glass and a rutile stoichiometric Ti concentration were used as an external standard and an internal standard, respectively, to calculate the trace element concentrations of unknowns. Data reduction was performed using the “Geochron_4” scheme of *Iolite*. The ^{207}Pb corrected $^{206}\text{Pb}/^{238}\text{U}$ ages of R13 and DX01 yielded a weighted average of 514 ± 8 Ma ($n = 22$; MSWD = 2.0) and 1809 ± 14 Ma ($n = 25$; MSWD = 3.0) during the analysis. Common Pb compositions of unknowns were corrected using an iterative approach based on a ^{207}Pb -correction of the terrestrial Pb evolution model (Chew et al., 2014). We applied a double iteration starting with a common $^{207}\text{Pb}/^{206}\text{Pb}$ composition of 0.836, from which point the change of the ^{207}Pb corrected ages between iterations is negligible. Low U contents or high Pb/U ratios of some rutile grains might cause negligible radiogenic Pb content contrast to common Pb, leading large age uncertainties. In order to get geological meaningful ages, we excluded analyses with ^{207}Pb -corrected age uncertainties (2σ) $>25\%$. Analyses with 2σ uncertainties up to 50% were permitted for rutile grains yielding ages younger than 100 Ma.

References:

- Andersen, T., 2002. Correction of common lead in U–Pb analyses that do not report ^{204}Pb . *Chemical Geology*, v. 192, p. 59–79.
- Cai, K., Sun, M., Jahn, B., Xiao, W., Yuan, C., Long, X., Chen, H., and Tumurkhuu, D., 2015, A synthesis of zircon U–Pb ages and Hf isotopic compositions of granitoids from Southwest Mongolia: Implications for crustal nature and tectonic evolution of the Altai Superterrane: *Lithos*, v. 232, p. 131–142, doi:10.1016/j.lithos.2015.06.014.
- Chen, Y., Song, S., Niu, Y., and Wei, C., 2014, Melting of continental crust during subduction initiation: A case study from the Chaidanuo peraluminous granite in the North Qilian suture zone: *Geochimica et Cosmochimica Acta*, v. 132, p. 311–336, doi:10.1016/j.gca.2014.02.011.
- Cheng, F., Jolivet, M., Hallot, E., Zhang, D., Zhang, C., and Guo, Z., 2017, Tectono-magmatic rejuvenation of the Qaidam craton, northern Tibet: *Gondwana Research*, v. 49, p. 248–263,

doi:10.1016/j.gr.2017.06.004.

Chew, D.M., Petrus, J.A., and Kamber, B.S., 2014, U–Pb LA–ICPMS dating using accessory mineral standards with variable common Pb: *Chemical Geology*, v. 363, p. 185–199.

Ding, Q.-F., Jiang, S.-Y., and Sun, F.-Y., 2014, Zircon U–Pb geochronology, geochemical and Sr–Nd–Hf isotopic compositions of the Triassic granite and diorite dikes from the Wulonggou mining area in the Eastern Kunlun Orogen, NW China: Petrogenesis and tectonic implications: *Lithos*, v. 205, p. 266–283, doi:10.1016/j.lithos.2014.07.015.

Ding, Q.-F., Liu, F., and Yan, W., 2015, Zircon U–Pb geochronology and Hf isotopic constraints on the petrogenesis of Early Triassic granites in the Wulonggou area of the Eastern Kunlun Orogen, Northwest China: *International Geology Review*, v. 57, p. 1735–1754, doi:10.1080/00206814.2015.1029541.

Dong, G., Luo, M., Mo, X., Zhao, Z., Dong, L., Yu, X., Wang, X., Li, X., Huang, X., and Liu, Y., 2018, Petrogenesis and tectonic implications of early Paleozoic granitoids in East Kunlun belt: Evidences from geochronology, geochemistry and isotopes: *Geoscience Frontiers*, v. 9, p. 1383–1397, doi:10.1016/j.gsf.2018.03.003.

Fisher, C.M., McFarlane, C.R.M., Hanchar, J.M., Schmitz, M.D., Sylvester, P.J., Lam, R., and Longerich, H.P., 2011, Sm–Nd isotope systematics by laser ablation-multicollector-inductively coupled plasma mass spectrometry: Methods and potential natural and synthetic reference materials: *Chemical Geology*, v. 284, p. 1–20, doi:10.1016/j.chemgeo.2011.01.012.

Fisher, C.M., Vervoort, J.D., and DuFrane, S.A., 2014, Accurate Hf isotope determinations of complex zircons using the “laser ablation split stream” method: *Geochemistry, Geophysics, Geosystems*, v. 15, p. 121–139.

Fisher, C.M., Paton, C., Pearson, D.G., Sarkar, C., Luo, Y., Tersmette, D.B., and Chacko, T., 2017, Data reduction of laser ablation split-stream (LASS) analyses using newly developed features within Iolite: With applications to Lu–Hf + U–Pb in detrital zircon and Sm–Nd + U–Pb in igneous monazite: *Geochemistry, Geophysics, Geosystems*, v. 18, p. 4604–4622.

Fisher, C.M., Bauer, A.M., Luo, Y., Sarkar, C., Hanchar, J.M., Vervoort, J.D., Tapster, S.R., Horstwood, M., and Pearson, D.G., 2020, Laser ablation split-stream analysis of the Sm–Nd and U–Pb isotope compositions of monazite, titanite, and apatite – Improvements, potential reference materials, and application to the Archean Saglek Block gneisses: *Chemical Geology*, v. 539, p.

119493, doi:10.1016/j.chemgeo.2020.119493.

Guo, Z.T., Peng, S.Z., Hao, Q.Z., Biscaye, P.E., and Liu, T.S., 2001, Origin of the Miocene–Pliocene Red-Earth Formation at Xifeng in Northern China and implications for paleoenvironments: *Palaeogeography, Palaeoclimatology, Palaeoecology*, v. 170, p. 11–26, doi:10.1016/S0031-0182(01)00235-8.

He, Z.-Y., Klemm, R., Yan, L.-L., and Zhang, Z.-M., 2018, The origin and crustal evolution of microcontinents in the Beishan orogen of the southern Central Asian Orogenic Belt: *Earth-Science Reviews*, v. 185, p. 1–14, doi:10.1016/j.earscirev.2018.05.012.

Kapp, P., Yin, A., Manning, C.E., Harrison, T.M., Taylor, M.H., and Ding, L., 2003, Tectonic evolution of the early Mesozoic blueschist-bearing Qiangtang metamorphic belt, central Tibet: *QIANGTANG METAMORPHIC BELT: Tectonics*, v. 22, p. n/a-n/a, doi:10.1029/2002TC001383.

Kapp, P., and DeCelles, P.G., 2019, Mesozoic–Cenozoic geological evolution of the Himalayan–Tibetan orogen and working tectonic hypotheses: *American Journal of Science*, v. 319, p. 159–254, doi:10.2475/03.2019.01.

Kozakov, I.K., Kovach, V.P., Bibikova, E.V., Kirnozova, T.I., Zagornaya, N.Y., Plotkina, Y.V., and Podkovyrov, V.N., 2007, Age and Sources of Granitoids in the Junction Zone of the Caledonides and Hercynides in Southwestern Mongolia: *Geodynamic Implications*: v. 15, p. 25.

Li, S., Wang, T., Wilde, S.A., and Tong, Y., 2013, Evolution, source and tectonic significance of Early Mesozoic granitoid magmatism in the Central Asian Orogenic Belt (central segment): *Earth-Science Reviews*, v. 126, p. 206–234, doi:10.1016/j.earscirev.2013.06.001.

Ludwig, K.R., 2012, *Isoplot/Ex Version 4.15: A Geochronological Toolkit for Microsoft Excel*: Berkeley Geochronology Center Special Publication, v. 5, 75 p.

Luvizotto, G.L. et al., 2009, Rutile crystals as potential trace element and isotope mineral standards for microanalysis: *Chemical Geology*, v. 261, p. 346–369, doi:10.1016/j.chemgeo.2008.04.012.

Peng, T., Zhao, G., Fan, W., Peng, B., and Mao, Y., 2015, Late Triassic granitic magmatism in the Eastern Qiangtang, Eastern Tibetan Plateau: *Geochronology, petrogenesis and implications for the tectonic evolution of the Paleo-Tethys: Gondwana Research*, v. 27, p. 1494–1508, doi:10.1016/j.gr.2014.01.009.

Petrus, J.A., and Kamber, B.S., 2012, *VizualAge: A Novel Approach to Laser Ablation ICP-MS U-Pb Geochronology Data Reduction*: *Geostandards and Geoanalytical Research*, v. 36, p. 247–270,

doi:10.1111/j.1751-908X.2012.00158.x.

Song, S., Bi, H., Qi, S., Yang, L., Allen, M.B., Niu, Y., Su, L., and Li, W., 2018, HP–UHP Metamorphic Belt in the East Kunlun Orogen: Final Closure of the Proto-Tethys Ocean and Formation of the Pan-North-China Continent: *Journal of Petrology*, v. 59, p. 2043–2060, doi:10.1093/petrology/egy089.

Sun, M., Yuan, C., Xiao, W., Long, X., Xia, X., Zhao, G., Lin, S., Wu, F., and Kröner, A., 2008, Zircon U–Pb and Hf isotopic study of gneissic rocks from the Chinese Altai: Progressive accretionary history in the early to middle Palaeozoic: *Chemical Geology*, v. 247, p. 352–383, doi:10.1016/j.chemgeo.2007.10.026.

Sun, M., Long, X., Cai, K., Jiang, Y., Wang, B., Yuan, C., Zhao, G., Xiao, W., and Wu, F., 2009, Early Paleozoic ridge subduction in the Chinese Altai: Insight from the abrupt change in zircon Hf isotopic compositions: *Science in China Series D: Earth Sciences*, v. 52, p. 1345–1358, doi:10.1007/s11430-009-0110-3.

Triebold, S., Luvizotto, G.L., Tolosana-Delgado, R., Zack, T., and von Eynatten, H., 2011, Discrimination of TiO₂ polymorphs in sedimentary and metamorphic rocks: *Contributions to Mineralogy and Petrology*, v. 161, p. 581–596.

Triebold, S., von Eynatten, H., and Zack, T., 2012, A recipe for the use of rutile in sedimentary provenance analysis: *Sedimentary Geology*, v. 282, p. 268–275, doi:10.1016/j.sedgeo.2012.09.008.

Wang, N., Wu, C.-L., Lei, M., and Chen, H.-J., 2018, Petrogenesis and tectonic implications of the Early Paleozoic granites in the western segment of the North Qilian orogenic belt, China: *Lithos*, v. 312–313, p. 89–107, doi:10.1016/j.lithos.2018.04.023.

Watson, E.B., Wark, D.A., and Thomas, J.B., 2006, Crystallization thermometers for zircon and rutile: *Contributions to Mineralogy and Petrology*, v. 151, p. 413.

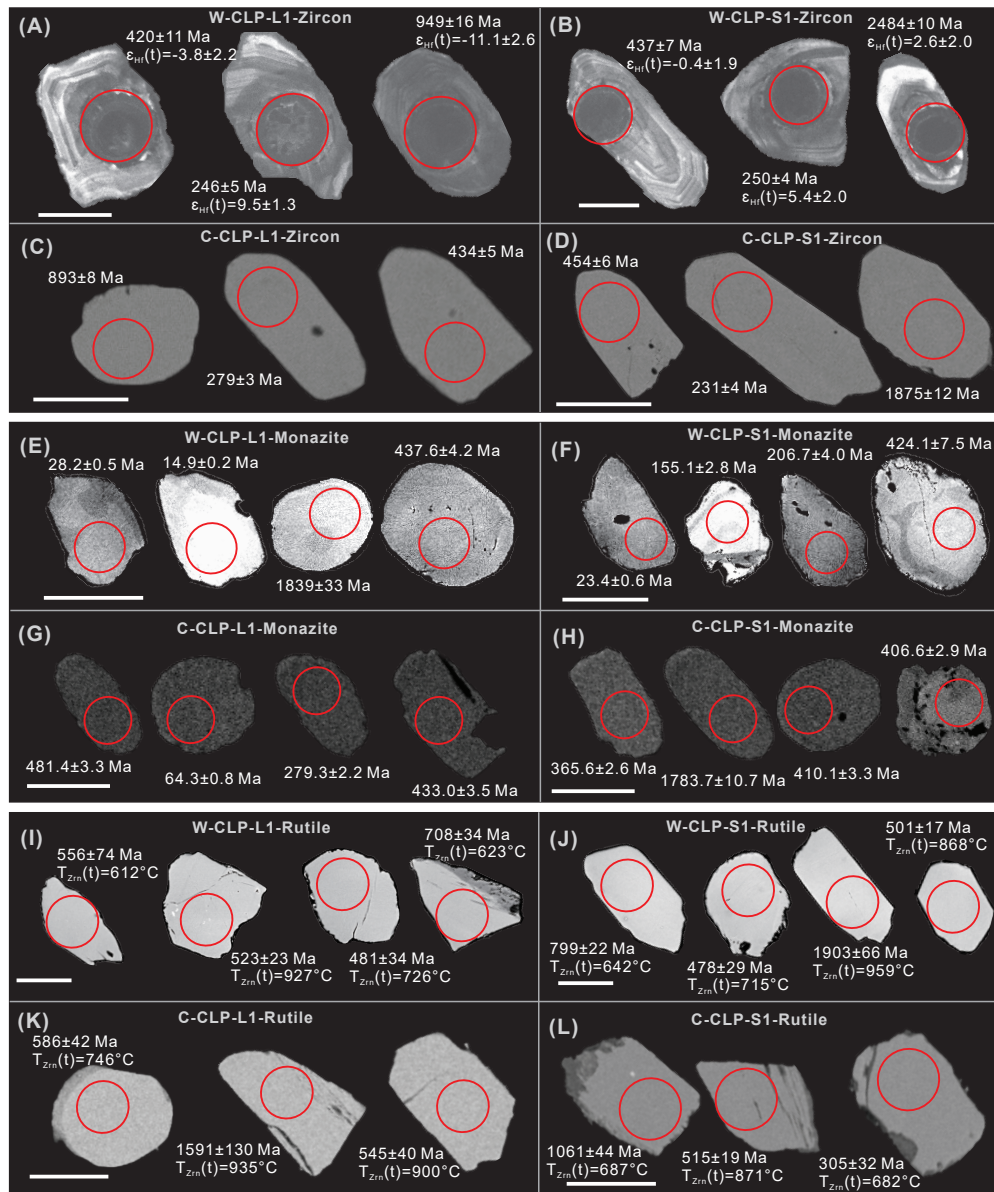
Wiedenbeck, M., Allé, P., Corfu, F., Griffin, W. I., Meier, M., Oberli, F., Quadt, A.V., Roddick, J. c., and Spiegel, W., 1995, Three Natural Zircon Standards for U-Th-Pb, Lu-Hf, Trace Element and Re Analysis: *Geostandards Newsletter*, v. 19, p. 1–23.

Xia, R., Wang, C., Qing, M., Li, W., Carranza, E.J.M., Guo, X., Ge, L., and Zeng, G., 2015, Zircon U–Pb dating, geochemistry and Sr–Nd–Pb–Hf–O isotopes for the Nan’getan granodiorites and mafic microgranular enclaves in the East Kunlun Orogen: Record of closure of the Paleo-Tethys: *Lithos*, v. 234–235, p. 47–60, doi:10.1016/j.lithos.2015.07.018.

- Xie, L., Zhang, Y., Zhang, H., Sun, J., and Wu, F., 2008, In situ simultaneous determination of trace elements, U-Pb and Lu-Hf isotopes in zircon and baddeleyite: *Chinese Science Bulletin*, v. 53, p. 1565–1573, doi:10.1007/s11434-008-0086-y.
- Xiong, F., Ma, C., Wu, L., Jiang, H., and Liu, B., 2015, Geochemistry, zircon U–Pb ages and Sr–Nd–Hf isotopes of an Ordovician appinitic pluton in the East Kunlun orogen: New evidence for Proto-Tethyan subduction: *Journal of Asian Earth Sciences*, v. 111, p. 681–697, doi:10.1016/j.jseae.2015.05.025.
- Yu, S., Zhang, J., Qin, H., Sun, D., Zhao, X., Cong, F., and Li, Y., 2015, Petrogenesis of the early Paleozoic low-Mg and high-Mg adakitic rocks in the North Qilian orogenic belt, NW China: Implications for transition from crustal thickening to extension thinning: *Journal of Asian Earth Sciences*, v. 107, p. 122–139, doi:10.1016/j.jseae.2015.04.018.
- Yuan, H.-L., Gao, S., Dai, M.-N., Zong, C.-L., Günther, D., Fontaine, G.H., Liu, X.-M., and Diwu, C., 2008, Simultaneous determinations of U–Pb age, Hf isotopes and trace element compositions of zircon by excimer laser-ablation quadrupole and multiple-collector ICP-MS: *Chemical Geology*, v. 247, p. 100–118, doi:10.1016/j.chemgeo.2007.10.003.
- Zhai, Q., Jahn, B., Su, L., Wang, J., Mo, X.-X., Lee, H., Wang, K., and Tang, S., 2013, Triassic arc magmatism in the Qiangtang area, northern Tibet: Zircon U–Pb ages, geochemical and Sr–Nd–Hf isotopic characteristics, and tectonic implications: *Journal of Asian Earth Sciences*, v. 63, p. 162–178, doi:10.1016/j.jseae.2012.08.025.
- Zhang, L.-Y. et al., 2014, Age and geochemistry of western Hoh-Xil–Songpan-Ganzi granitoids, northern Tibet: Implications for the Mesozoic closure of the Paleo-Tethys ocean: *Lithos*, v. 190–191, p. 328–348, doi:10.1016/j.lithos.2013.12.019.
- Zhao, G., Wang, Y., Huang, B., Dong, Y., Li, S., Zhang, G., and Yu, S., 2018, Geological reconstructions of the East Asian blocks: From the breakup of Rodinia to the assembly of Pangea: *Earth-Science Reviews*, v. 186, p. 262–286, doi:10.1016/j.earscirev.2018.10.003.
- Zhou, B., Dong, Y., Zhang, F., Yang, Z., Sun, S., and He, D., 2016, Geochemistry and zircon U-Pb geochronology of granitoids in the East Kunlun Orogenic Belt, northern Tibetan Plateau: origin and tectonic implications: *Journal of Asian Earth Sciences*, v. 130, p. 265–281, doi:10.1016/j.jseae.2016.08.011.
- Zuza, A.V., Wu, C., Reith, R.C., Yin, A., Li, J., Zhang, J., Zhang, Y., Wu, L., and Liu, W., 2018,

Tectonic evolution of the Qilian Shan: An early Paleozoic orogen reactivated in the Cenozoic: GSA
Bulletin, v. 130, p. 881–925, doi:10.1130/B31721.1.

Fig. S1



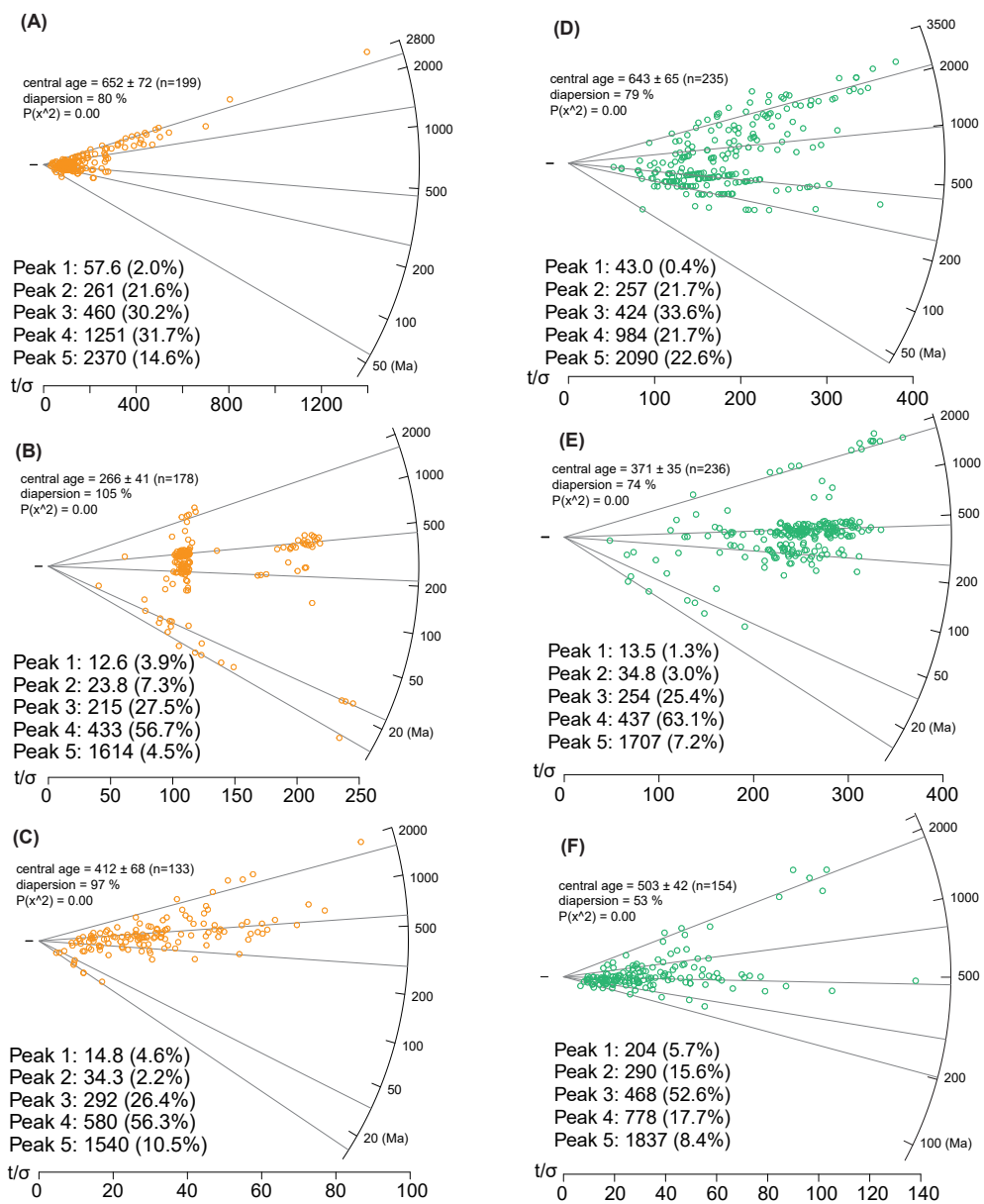
Supplementary Fig. 1 Representative cathodoluminescence images of detrital zircon grains from samples W-L1 (A) and W-S1 (B); backscattered electron images of detrital zircon grains from samples C-L1 (C) and C-S1 (D), monazite grains from samples W-L1, -S1 (E, F) and C-L1, -S1 (G, H), and rutile grains from samples W-L1, -S1 (I, J) and C-L1, -S1 (K, L). Red circles indicate positions of laser ablation sites with their corresponding ages, $\epsilon_{Hf}(t)$ values and Zr-in-rutile thermometry (T_{Zrn}). The white bars indicate 50 μm in scale.

Fig. S2



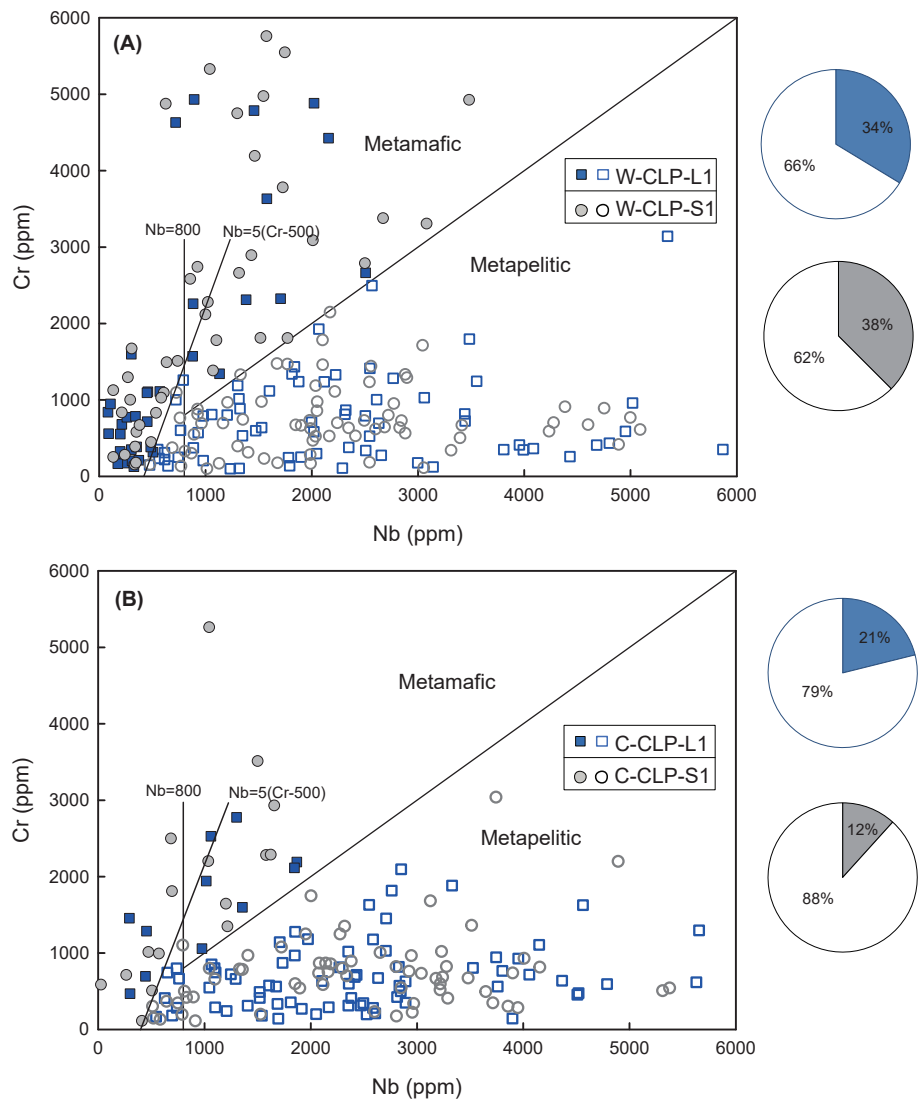
Supplementary Fig. 2 Field photos of the sampling sections in the western CLP; (A) W-L1, Wuchuancun and (B) W-S1, Qianjiatai.

Fig. S3



Supplementary Fig. 3 Radial plots and mixture modelling results of adopted U/Th-Pb ages using IsoplotR. Zircon (A), monazite (B) and rutile (C) from the samples in the western CLP. Zircon (D), monazite (E) and rutile (F) from the samples in the central CLP.

Fig. S4



Supplementary Fig. 4 Nb vs. Cr plots for discrimination of metamafic and metapelitic rutile for the western CLP samples (A) and central CLP samples (B) (after Triebold et al. 2012). Right panels show the corresponding pie charts.